Available online at www.sciencedirect.com
SCIENCE DIRECT
International Journal of Heat and Mass Transfer 49 (2006) 2265–2276
International Journal of HEAT and MASS TRANSFER
www.elsevier.com/locate/ijhmt

Pattern formation of drops in thermocapillary migration

S. Nas [a], M. Muradoglu [b,*], G. Tryggvason [c]

[a] Department of Aeronautical and Astronautical Engineering, Istanbul Technical University, Maslak, Istanbul 34469, Turkey
[b] Department of Mechanical Engineering, Koc University, Sariyer, Istanbul 34450, Turkey
[c] Department of Mechanical Engineering, Worcester Polytechnic Institute, Worcester, MA 01609-2280, USA

Received 22 December 2004; received in revised form 19 July 2005
Available online 28 February 2006

Abstract

The behavior of a drop cloud in thermocapillary motion in zero gravity is examined for both mono-dispersed and poly-dispersed cases. Numerical simulations of the thermocapillary motion of two- and three-dimensional fully deformable light drops are presented. The Navier–Stokes equations coupled with the energy conservation equation are solved by a front-tracking/finite-difference method. The material properties of the drop fluid and the ambient fluid are different, and the interfacial tension depends on the temperature. At moderate Reynolds (*Re*) and Marangoni (*Ma*) numbers, the results show that drops form layers nearly perpendicular to the temperature gradient.

Keywords: Thermocapillary migration; Zero gravity; Pattern formation; Front-tracking method

1. Introduction

It is well known that drops suspended in a fluid with a temperature field move in the direction of the temperature gradient due to thermocapillary forces. Interfacial tension generally decreases with increasing temperature and a non-uniform temperature field in the ambient fluid generates an interfacial tension gradient at the fluid interface that, in turn, induces shear stresses acting on the outer fluid by viscous forces, and thus inducing a motion of the drop in the direction of the temperature gradient. This phenomenon is known as the thermocapillary migration of drops and it can play an important role in material processing under the microgravity condition in the space as well as in many other scientific and engineering applications.

Following the pioneering work of Young et al. [14] who found an analytical expression for the terminal velocity of a single spherical drop in the creeping flow limit, the behavior of a single fluid particle in a temperature gradient has been extensively studied and been reasonably well understood. However, it is frequently necessary to deal with a large number of drops and their collective behavior may differ substantially from the thermocapillary migration of a single isolated drop. The thermocapillary motion of two drops and their interactions were first examined analytically by Anderson [1] in the limit of zero Reynolds and Marangoni numbers. Anderson [1] showed that the collective behavior of a droplet suspension is considerably different from that of a single isolated drop. This result was then confirmed by Keh and Chen [3] who studied axisymmetric thermocapillary migration of two spherical droplets in a creeping flow regime. Keh and Chen [4] also investigated the axisymmetric thermocapillary motion of a chain of spherical droplets in a quasi-steady state limit of conservation of energy and momentum using a combined analytical–numerical method. The interaction of dispersed spherical drops in thermocapillary motion was examined by Zhang and Davis [16] in creeping flow conditions with a trajectory method. Keh and Chen [5] studied the

* Corresponding author.
E-mail addresses: nas@itu.edu.tr (S. Nas), mmuradoglu@ku.edu.tr (M. Muradoglu), gretar@wpi.edu (G. Tryggvason).

0017-9310/$ - see front matter © 2006 Elsevier Ltd. All rights reserved.
doi:10.1016/j.ijheatmasstransfer.2005.12.009

Nomenclature

a	initial drop radius (m)	We	Weber number ($\rho_o a U_r^2/\sigma_o$)
a_v	average drop radius (m)	α	thermal diffusivity ($k/\rho c_p$)
c_p	specific heat capacity (J/kg K)	γ	deformation
c_p^*	ratio of heat capacity (c_{p_i}/c_{p_o})	ϵ	deformation parameter
i	subscript denoting drop fluid	μ	dynamic viscosity (N s/m^2)
k	heat conduction coefficient (W/m K)	μ^*	viscosity ratio (μ_i/μ_o)
k^*	ratio of heat conduction coefficient (k_i/k_o)	ν	kinematic viscosity (m^2/s)
Ma	Marangoni number ($U_r a/\alpha_o$)	ρ	density (kg/m^3)
o	subscript denoting ambient fluid	ρ^*	density ratio (ρ_i/ρ_o)
Re	Reynolds number ($U_r a/\nu_o$)	σ	interfacial tension coefficient (N/m)
T_o	reference temperature (K)	σ_o	interfacial tension coefficient at T_o
t_r	reference time scale (a/U_r)	σ_T	proportionality coefficient ($-\mathrm{d}\sigma/\mathrm{d}T$)
U_r	reference velocity ($\sigma_T a\lvert\nabla T_\infty\rvert/\mu_o$)	∇T_∞	temperature gradient in undisturbed ambient fluid
U_{rv}	average reference velocity (m/s)		

interaction of many droplets in the limit of creeping thermocapillary motion and found that the terminal velocity of gas bubbles is independent of each other if they are all equal in size in the limiting case of zero Reynolds and Marangoni numbers. Nas and Tryggvason [9] studied the interaction of two droplets at moderate Reynolds and Marangoni numbers and showed that, in contrast with the results found in the creeping flow limit, the terminal velocity of droplets can be strongly affected by the presence of other droplets depending on the separation distance between them. The reader is referred to the review papers by Subramanian [10] and by Wozniak et al. [15] and to a recent book by Subramanian and Balasubramaniam [11] for a detailed discussion of analytical, numerical and experimental methods about the thermocapillary motion of drops in reduced gravity including a more complete list of literature on the subject.

The investigations of interactions of drops discussed above have mostly been limited to zero Reynolds and Marangoni numbers. In many engineering applications where thermocapillary forces are dominant, it is likely that many drops are present and heat and mass convections are important, i.e., Reynolds and Marangoni numbers are non-zero. It is therefore critical to understand the overall behavior of large drop systems with either mono-dispersed or poly-dispersed cases including the effect of non-zero Reynolds and Marangoni numbers. In the present work, numerical simulation of equal size (mono-dispersed) drops as well as unequal size (poly-dispersed) drops in two and three dimensions are presented for non-zero values of Reynolds and Marangoni numbers. It is found that the drops align themselves nearly perpendicular to the temperature gradient. This might be an important result since it suggests that the formation of drop layers may result in dislocations inside the solidified material produced in microgravity environment.

2. Formulation and numerical method

The governing equations are described in this section in the framework of the front-tracking method. In this method, the flow equations are written for the entire flow field and different phases are treated as a single fluid with variable material properties. A detailed description and numerical properties of the front-tracking/finite-difference method can be found in the review paper by Tryggvason et al. [12] where some results for the thermocapillary migration of drops are also presented. In addition, the formulated governing equations and the numerical solution method employed here for the computations of thermocapillary migration of drops are the same as described by Nas and Tryggvason [9]. Some validation results and an extensive computational study of the thermocapillary motion of a single drop and two drop interactions can also be found in Nas and Tryggvason [9].

2.1. Governing equations

As mentioned above, it is possible to write the Navier–Stokes equations as a single set of equations for the whole domain as long as the jumps in fluid properties are correctly accounted for and interfacial tension is included. The Navier–Stokes equations in conservative form are given by

$$\frac{\partial \rho \mathbf{u}}{\partial t} + \nabla \cdot (\rho \mathbf{u}\mathbf{u}) = -\nabla p + \nabla \cdot \mu(\nabla \mathbf{u} + \nabla \mathbf{u}^{\mathrm{T}}) + \int \delta^{\beta}(\mathbf{x} - \mathbf{x}_{\mathrm{f}}) \frac{\partial}{\partial s}(\sigma \mathbf{t})\mathrm{d}s, \tag{1}$$

where the last term is the interfacial tension acting on the interface, included as a body force by representing it as a delta function. Here $\mathbf{u}$ is the velocity field, p is the pressure,

ρ is the density, μ is the viscosity, σ is the interfacial tension, $\mathbf{t}$ is a unit tangent vector, s is the arc length along the interface or along the edge of the surface element, $\mathbf{x}_f$ is the position of the interface, and the integral is over the interface separating the fluids. δ^β is a two dimensional ($\beta = 2$) or three dimensional ($\beta = 3$) delta function, constructed by a repeated multiplication of one-dimensional δ functions.

The conservation of energy can be formulated as

$$\rho c_p \left(\frac{\partial T}{\partial t} + \nabla \cdot \mathbf{u} T \right) = \nabla \cdot (k \nabla T), \tag{2}$$

where T is the temperature and k and c_p are the coefficients of heat conduction and heat capacity, respectively, and heat generation is assumed to be negligible. Both fluids are immiscible and the material properties are constant in each fluid. Therefore, the equations of state for density, viscosity, heat capacity, and heat conduction are

$$\frac{D\rho}{Dt} = 0; \quad \frac{D\mu}{Dt} = 0; \quad \frac{Dk}{Dt} = 0; \quad \frac{Dc_p}{Dt} = 0, \tag{3}$$

where $\frac{D}{Dt} = \frac{\partial}{\partial t} + \mathbf{u} \cdot \nabla$ is the substantial derivative. The incompressibility constraint gives a solenoidal velocity field

$$\nabla \cdot \mathbf{u} = 0. \tag{4}$$

A non-separable elliptic equation for the pressure is found by combining the momentum equation and the incompressibility condition, and is solved numerically together with the momentum and energy equations.

2.2. Numerical method

The numerical technique employed here is the front-tracking/finite-difference method developed by Unverdi and Tryggvason [13]. The flow equations are solved using a fixed, regular, staggered grid. The momentum equations are discretized using a conservative, second-order central difference scheme for the spatial variables and an explicit predictor–corrector, second-order projection scheme is used for the time-integration. The interface is represented by discrete computational points or triangular elements that are moved by the fluid velocity interpolated from the fixed grid. These points or elements are connected to form a front that is used to keep the density and viscosity stratification sharp, and to calculate the interfacial tension. The pressure equation is non-separable since the density varies and a multigrid method is used to solve it efficiently.

In two-dimensional simulations, the net interfacial tension force on each element is found directly by

$$\mathbf{F}_s = \oint_{\text{elem}} \frac{\partial}{\partial s} (\sigma \mathbf{t}) \mathrm{d}s = (\sigma \mathbf{t})_2 - (\sigma \mathbf{t})_1, \tag{5}$$

where the unit tangent vector $\mathbf{t}$ is computed by fitting a Legendre polynomial to the end-points of each element and the end points of the adjacent elements. For a three dimensional flow, this force is found by

$$\mathbf{F}_s = \int_{\nabla S} \sigma \mathbf{t} \times \mathbf{n} \mathrm{d}S. \tag{6}$$

Here $\mathbf{t}$ is a unit tangent vector along the edge of the triangular surface element, and $\mathbf{n}$ is a unit normal vector to the same triangular surface element. The integral is performed over the surface of the front element. This formulation has some advantages as discussed by Tryggvason et al. [12].

An indicator function is defined such that it is unity inside the droplet and zero outside. Based on the locations of the interface marker points, unit magnitude jumps are distributed in a conservative manner on the computational grid points near the interface and are integrated to compute the indicator function everywhere. This procedure involves solution of a separable Poisson equation and yields a smooth transition of the indicator function across the interface. Once the indicator function distribution is determined, the fluid properties such as viscosity and density are set as a function of the indicator function.

The readers are referred to the references by Tryggvason et al. [12] and by Nas and Tryggvason [9] for a detailed description of the numerical method.

2.3. Validation test

The accuracy of the method is tested for a simple flow in this section. For this purpose, a strip of one fluid is laid down in a channel and is surrounded by an ambient fluid. A schematic is shown in Fig. 1. The domain is wall bounded in the vertical direction and periodic in the horizontal direction. There are two interfaces at the top and the bottom of the symmetry axis x. The density of the middle layer is equal to the outer one, but its viscosity is half of the outer one. It is assumed that the temperature field is fully developed and increases linearly with x. Since the interfacial tension is a function of temperature, the only force acting on each interface is the interfacial tension gradient along the interface, σ_x. The governing equation for this flow can be written as

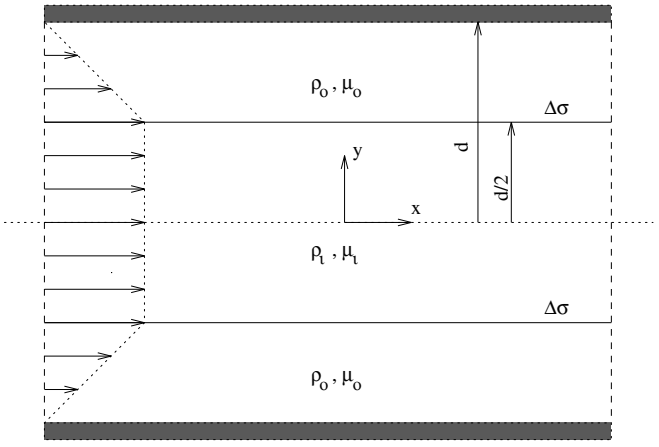

Fig. 1. Schematic of the validation test problem.

$$\frac{\mathrm{d}}{\mathrm{d}y}\left(\mu\frac{\mathrm{d}u}{\mathrm{d}y}\right)+\sigma_x\delta(y)=0, \tag{7}$$

where u is the x component of the velocity. The solution of Eq. (7) is subject to the no-slip boundary condition on the walls and zero velocity gradient at the axis of symmetry. At each interface, the jump in shear stresses is balanced by the interfacial tension forces. The analytical solution can easily be found as

$$u(y)=\begin{cases}2\sigma_x d/\mu_o(1-|y|/d) & \text{if } d/2<|y|<d,\\ \sigma_x d/\mu_o & \text{if } |y|<d/2.\end{cases} \tag{8}$$

By integrating the velocity across the channel, the total mass flux is then given by

$$Q_{ex}=\frac{3}{4}\frac{\sigma_x d^2}{\mu_o}. \tag{9}$$

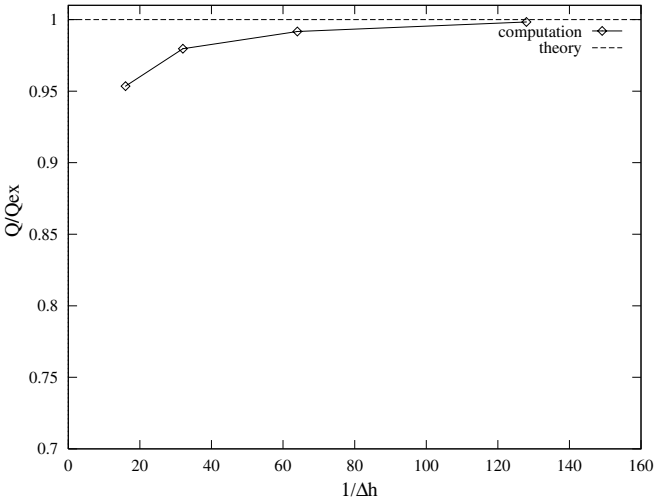

Fig. 2. Resolution test for the validation problem in Fig. 1. Total mass flux scaled by the exact mass flux versus grid resolution.

To demonstrate the accuracy of the numerical method, the total mass flux computed using different spatial grid resolutions is compared with the analytical solution given by Eq. (9) when the flow becomes fully developed, i.e., it reaches a steady state. Fig. 2 shows the computed mass flux normalized by the analytical solution for different grid resolutions. The computations are performed on a 1×1 rectangular domain and using various computational grids containing 16×16, 32×32, 64×64 and 128×128 grid points. It is clearly seen in this figure that the computed mass flux converges to the exact solution as the grid is refined, demonstrating the accuracy of the method. Some more validation tests for the present method can be found in Nas [8].

3. Results and discussion

The computational domain is taken to be periodic in the horizontal direction and bounded by rigid walls in the vertical direction. The top wall is hot and the bottom wall is cold, and initially the temperature varies linearly in the vertical direction.

All the results presented here are obtained on uniform Cartesian grids. In both two- and three-dimensional computations, the top and bottom boundaries are treated as no-slip walls at constant temperatures. Periodic boundary conditions are used in other directions for the flow and temperature fields. Initially, the drops are taken as infinitely long circular cylinders and spheres in two- and three-dimensional cases, respectively. The fluid is initially stationary and the temperature increases linearly from the cold bottom wall toward the hot top wall. The accuracy of the method with respect to the grid convergence has been shown by Nas and Tryggvason [9] and it has been found that the drops deform very little and about 32 grid points in each direction per drop diameter are sufficient to reduce the spatial error below 2%. It is therefore

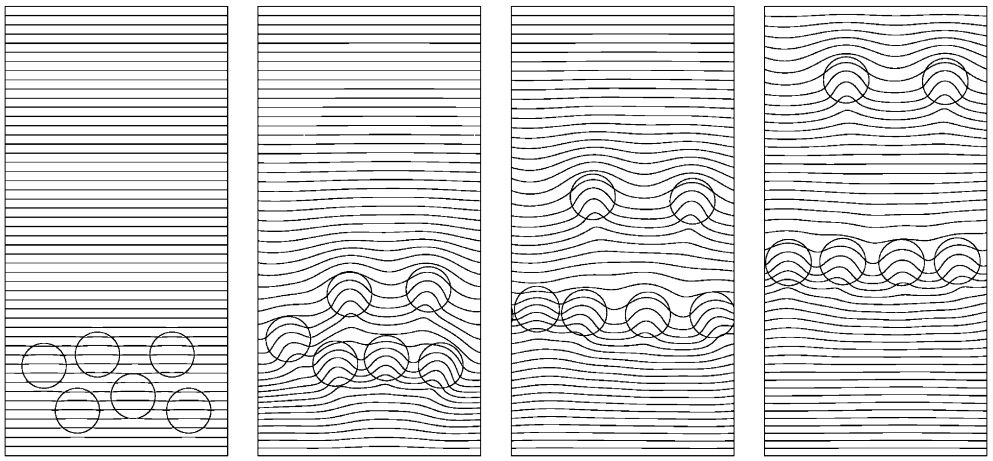

Fig. 3. Isotherms for selected frames from the computation of six drop interaction. Time progresses from left to right and 50 equally spaced contours are shown. The non-dimensional times (t^*) are 0.25, 25, 62.5, 112.5. The non-dimensional parameters are $Re=5$, $Ma=20$, $We=0.0833$ and material property ratios are 0.5.

assumed that the same resolution is sufficient for many drop simulations presented in this work. The details of the grid convergence studies have been reported in Nas and Tryggvason [9] and in Tryggvason et al. [12].

The flow evolution is controlled by the radius of the initially spherical drop a, the interfacial tension σ, the viscosity μ, the density ρ, the coefficient of heat capacity c_p, the coefficient of heat conduction k, and the temperature gradient in the ambient fluid far from the fluid particle ∇T_∞. The interfacial tension is assumed to be a linearly decreasing function of the temperature,

$$\sigma = \sigma_o + \sigma_T(T_o - T), \tag{10}$$

where T is the temperature and σ_o is the interfacial tension at reference temperature T_o and the coefficient is defined as

$$\sigma_T = -\frac{d\sigma}{dT} = \text{constant}. \tag{11}$$

The governing non-dimensional parameters are given by

$$Ma = \frac{U_r a}{\alpha_o}, \quad Re = \frac{U_r a}{\nu_o}, \quad We = \frac{\rho_o a U_r^2}{\sigma_o},$$
$$\rho^* = \frac{\rho_i}{\rho_o}, \quad \mu^* = \frac{\mu_i}{\mu_o}, \quad c_p^* = \frac{c_{p_i}}{c_{p_o}}, \quad k^* = \frac{k_i}{k_o}, \tag{12}$$

where $U_r = \frac{\sigma_T a}{\mu_o}|\nabla T_\infty|$ is the reference velocity, $t_r = a/U_r$ is the reference time scale, $\alpha_o = k_o/(\rho_o c_{p_o})$ is the thermal diffusivity and $\nu_o = \mu_o/\rho_o$ is the kinematic viscosity. *Ma*, *Re* and *We* are the Marangoni, Reynolds and Weber numbers, respectively. Note that the material properties of the drop fluid are denoted by the subscript "i" and the properties of the ambient fluid are denoted by the subscript "o".

The thermocapillary migration and interactions of mono-dispersed drops in a cloud are first examined and then the poly-dispersed drop systems are considered. It is shown by Meyyapan et al. [6] and Meyyapan and Subramanian [7] that the presence of planar surface

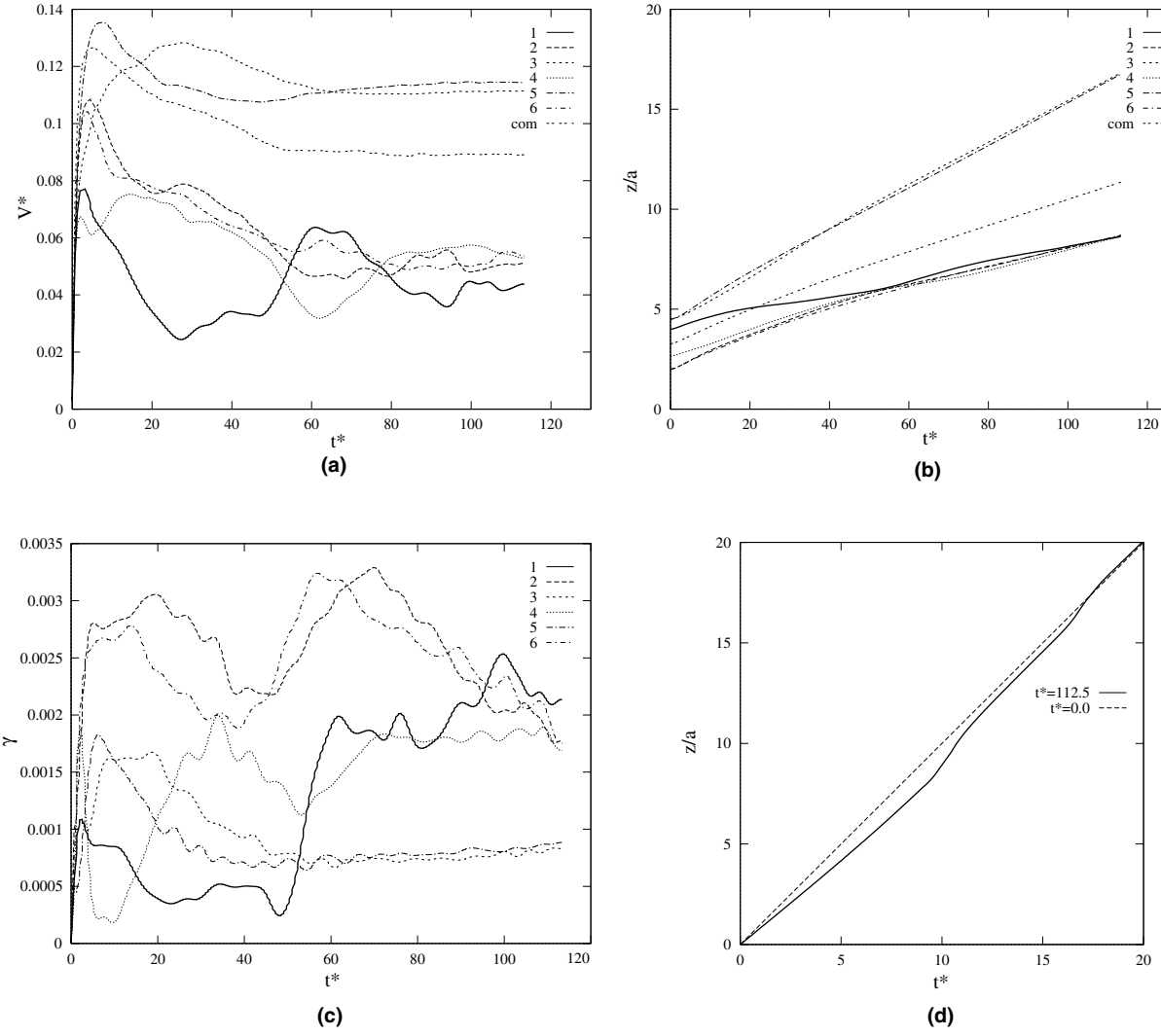

Fig. 4. The six two-dimensional equal size drop interaction. Drops marked 1–6 from left to right in the domain and "com" denotes the velocity of the center of mass of drop system. (a) Migration velocities versus time. (b) z component of the centroid of drops versus time. (c) Deformation versus time. (d) The average temperature distribution across the channel (solid line) and the initial temperature distribution (dashed line).

reduces the migration velocity of a bubble in a creeping flow regime when its distance to the wall is less than three drop radii. Chen and Keh [2] confirmed the same results for the case of drops. Considering the computational cost, the drops are initially placed arbitrarily but about two to three drop radii away from the lower wall in the present study and the simulations are terminated before any drop gets closer to the top wall more than two drop radii. This probably introduces some wall effects in the present computational results but these effects are expected to be small. Furthermore, the wall effects are also present in many applications.

3.1. Mono-dispersed drops

To investigate the interaction of many drops, the evolution of six drops is first computed. The computational domain is $10a$ long in x-direction and extends to $20a$ in z-direction and, is resolved by 128×256 grid points. The non-dimensional numbers for this case are $Re = 5$, $Ma = 20$, $We = 0.0833$ while the material property ratios are set to 0.5.

Fig. 3 shows the isotherms in the laboratory frame at different time frames. It is seen from the plots that two drops separate from the rest and move ahead, while the others start lining up across the channel. Later on, the two leading drops move side by side and migrate almost independently from the other drops. Fig. 4 shows the migration velocity, vertical positions of drop centroids, the deformation of drops and the average temperature distribution at the time of the last frame together with the initial temperature distribution. Note that the deformation is defined as

$$\gamma = \frac{1-\epsilon}{1+\epsilon}, \tag{13}$$

where

$$\epsilon = \frac{\text{minor axis of the drop}}{\text{major axis of the drop}}. \tag{14}$$

Examining the velocity of each drop in Fig. 4(a), it is clear that the velocity of the center of mass of the drop cloud reaches a steady state, while each individual drop does not. In particular, each drop in the group of four has oscillating migration velocities. Also, the leading drops move faster than the four drops left behind. Two faster drops quickly separate from the rest and each group lines up across the channel as seen in Fig. 4(b). Since the leading two drops move apart horizontally, their deformation is small at steady state compared with the other ones which are squeezed across the channel as seen in Fig. 4(c). The drops carry cold fluid with them upward and warmer fluid flows back between them to conserve mass. Since the thermal capacity of the drops is less than that of the outer fluid, the net effect is to heat the region around and behind the drops. As seen in Fig. 4(d), the temperature increases above the linear temperature profile at the location of two leading drops and increases even more across the bottom four drops. Since the temperature of the bottom wall is fixed, the temperature gradient in the bottom region must increase, which is verified by the close spacing of the isotherms shown in Fig. 3.

To investigate whether the layer formation suggested by the simulations presented above is a prominent feature in large drop clouds, simulations are performed using 16 equal size 2D drops placed in a $11.43a \times 11.43a$ domain.

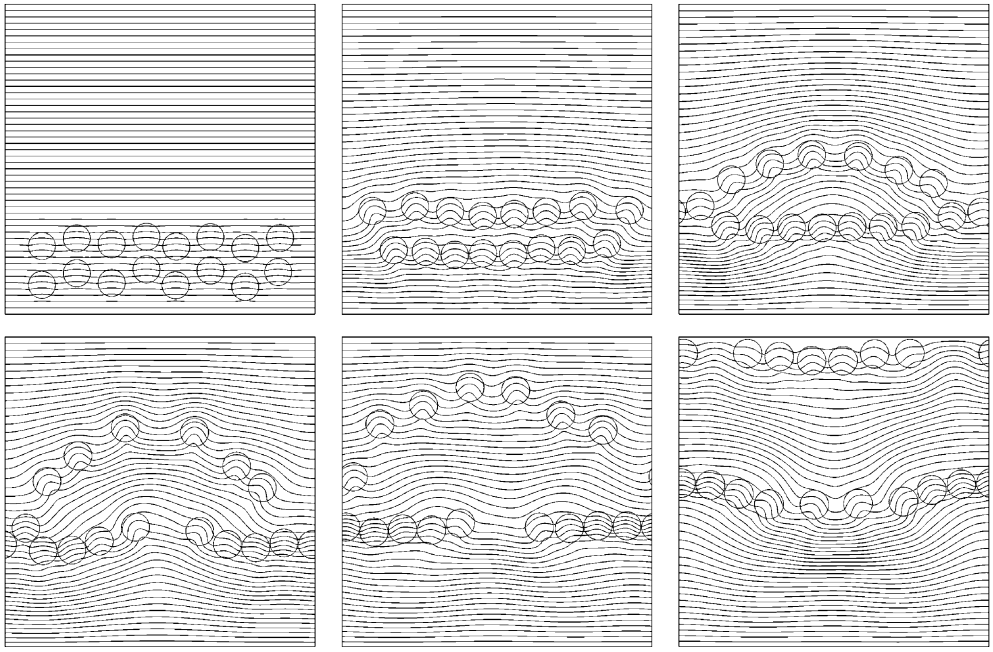

Fig. 5. Isotherms for selected frames from the simulation of 16 two-dimensional equal size drop interaction. Time progresses from left to right, top to bottom and 50 equally spaced contours are shown. The non-dimensional times (t^*) are 1.4, 64.3, 142.85, 214.3, 285.7, 428.6. The non-dimensional parameters are $Re = 5$, $Ma = 20$, $We = 0.0833$ and material property ratios are 0.5.

The computational domain is resolved by 256×256 grid points and the non-dimensional numbers are the same as in the six-drop simulation case. Fig. 5 shows the isotherms at different time frames. It can be seen from this figure that the drops form two layers. Since the sides of the domain are not occupied by drops, the hot ambient fluid flows down in this region. Since drops are close to each other in the top layer, the downward flow of ambient fluid is decreased. As a result of this behavior, the drops in the top layer move toward the sides of the domain and the first layer opens up like an envelope. As the top layer moves, the whole picture is nearly symmetric with respect to the middle vertical line. The drops in the top layer carry the cold fluid with them, forming a cold region between the two layers. Later on, the top layer breaks up, allowing the hot ambient fluid to flow down between the drops. Similarly, the lower layer also breaks up into two nearly horizontal layers due to the temperature gradient in the cold region between the two layers. After the break up, the hot ambient fluid flows down quickly in the middle of the domain. This causes the fluid to heat up in that region, changing the temperature gradient. By moving in the direction of the temperature gradient, the drops change direction toward the vertical middle symmetry line. The leading drops form a nearly horizontal layer before hitting the wall while the rest of the drops form another layer by coming close together horizontally due to the temperature gradient. This simulation suggests that while layers may form, they will break up through instability waves many times longer than the drop diameter, but eventually they strive to form stable layers. To demonstrate the formation of drop layers, the migration velocity and the vertical position of each drop centroid are plotted in Fig. 6. The drops in the top layer move faster than the drops in the lower layer until feeling the influence of the top wall, i.e., t^* is about 350 as seen in Fig. 6(a). It is interesting to observe that two drops which are initially in the top row have negative velocities during the period of approximately $t^* = 100$ and $t^* = 200$. One of these drops later joins the lower layer while the other accelerates and catches up with the drops in the upper layer. The formation of two layer structure can be seen more clearly from the evolution of the vertical locations of the drop centroids as shown in Fig. 6(b).

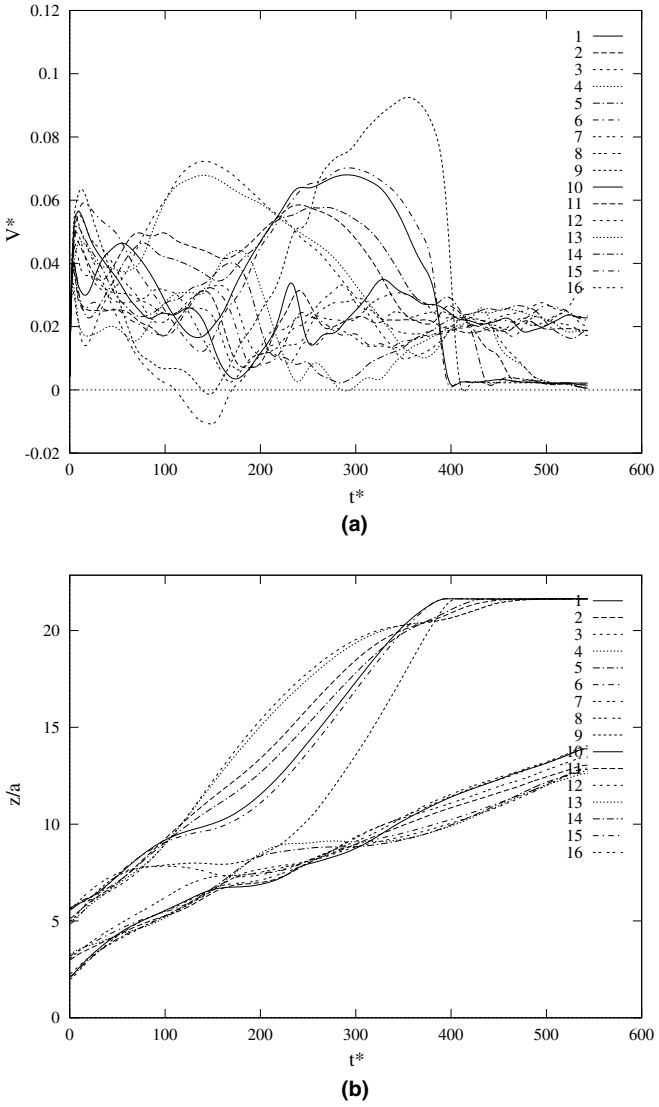

Fig. 6. The 16 two-dimensional equal size drop interaction. (a) Migration velocities versus time. (b) z component of the centroid of drops versus time.

After two-dimensional simulations of drop clouds, fully three-dimensional simulations are also performed. A three-dimensional simulation with a resolution of $64 \times 64 \times 128$ grid points is performed in a domain which extends 6.66 drop radii in x- and y-directions and twice as large in the z-direction. The non-dimensional numbers are the same as the two-dimensional simulations for 6 and 16 drop cases. Nine equal size drops are placed arbitrarily but initially close to the lower cold wall.

The migration of these drops toward the top hot wall at different time frames is shown in Fig. 7(a). Since the visualization of the isotherms is not as easy as it is in two-dimensions, the isotherms are shown over the middle cross-sectional plane. The isotherms are plotted in the middle $y - z$ plane in Fig. 7(b). It is seen from the isotherms that two drops form a layer by coming side by side while migrating toward the top wall. Since the isotherms on a cross-sectional plane is plotted, only a portion of this layer formation is seen, which actually involves more than two drops. The wake of the drops perturbs the temperature field only slightly. The isotherms wrap around the drops showing the level of convective transport of energy. Initially, the drops are close to each other and as they move toward the hot wall, one of the drops separates and moves faster than the other two drops which migrate almost side by side. The migration velocities and the vertical locations of drop centroids are plotted in Fig. 8. It can be seen more clearly from these figures that one of the nine drops separates from the other drops and the others form a layer similar to what is observed in the two-dimensional

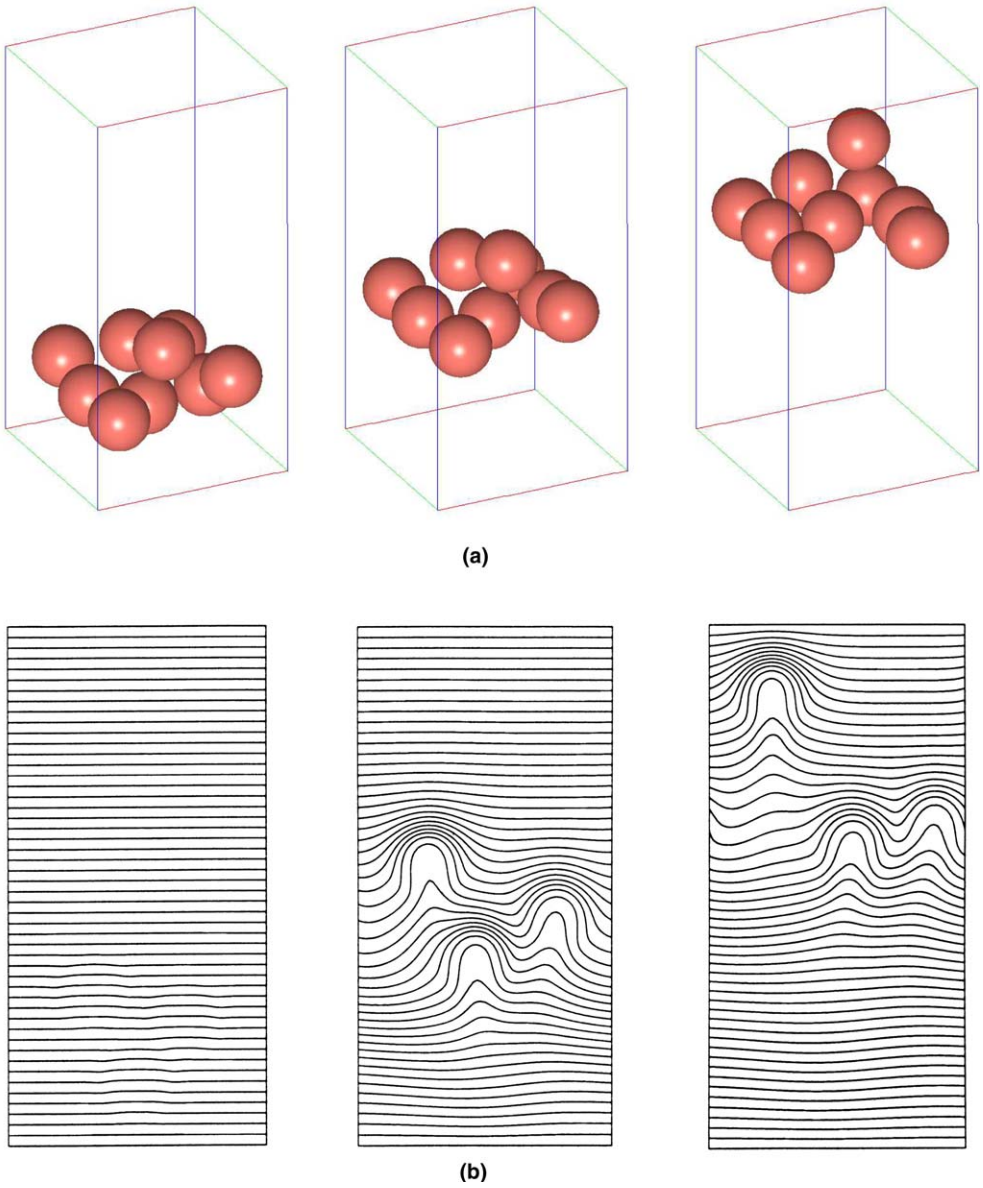

Fig. 7. A fully three-dimensional simulation of the interaction of nine equal size drops (top plots) and temperature contours for selected time frames with 50 equally spaced contours shown in the middle plane of the computational domain in x-direction (bottom plots). Time progresses from left to right. The non-dimensional times (t^*) are 0.66, 40, 86.66. Computational domain is $(x/a, y/a, z/a) = (6.66, 6.66, 13.33)$. The non-dimensional numbers are $Re = 5$, $Ma = 20$, $We = 0.0833$ and the material property ratios are 0.5.

simulations. The number of drops is just sufficient to form one nearly horizontal layer. The migration velocities of the drops clearly indicate that one of the drops, which was originally ahead of others, separates easily from the rest. These fully three-dimensional simulations confirm the formation of drop layers observed in the two-dimensional simulations.

3.2. Poly-dispersed drops

Drops of exactly the same size are unlikely to be present in real systems. Here, the interaction between drops with different sizes is explored by both two- and three-dimensional simulations.

The interaction among six drops is first examined. Three of the six drops are small and the other three are large. The ratio of the small drop radius to the large drop radius is $\lambda = 3/5$. An average drop radius, a_v, is defined by taking an arithmetic average of the radius of the drops. The average reference velocity, U_{rv}, is defined based on this average drop radius. The non-dimensional numbers for the big drops are the same as for the six-drop simulation in the mono-dispersed case, i.e., $Re = 5$, $Ma = 20$, $We = 0.0833$ and the material property ratios are 0.5. The resolution is 128×256 grid points in a $x/a_v = 10$, $z/a_v = 20$ computational domain.

The isotherms from this simulation at different time frames are shown in Fig. 9. It is seen that the drops come

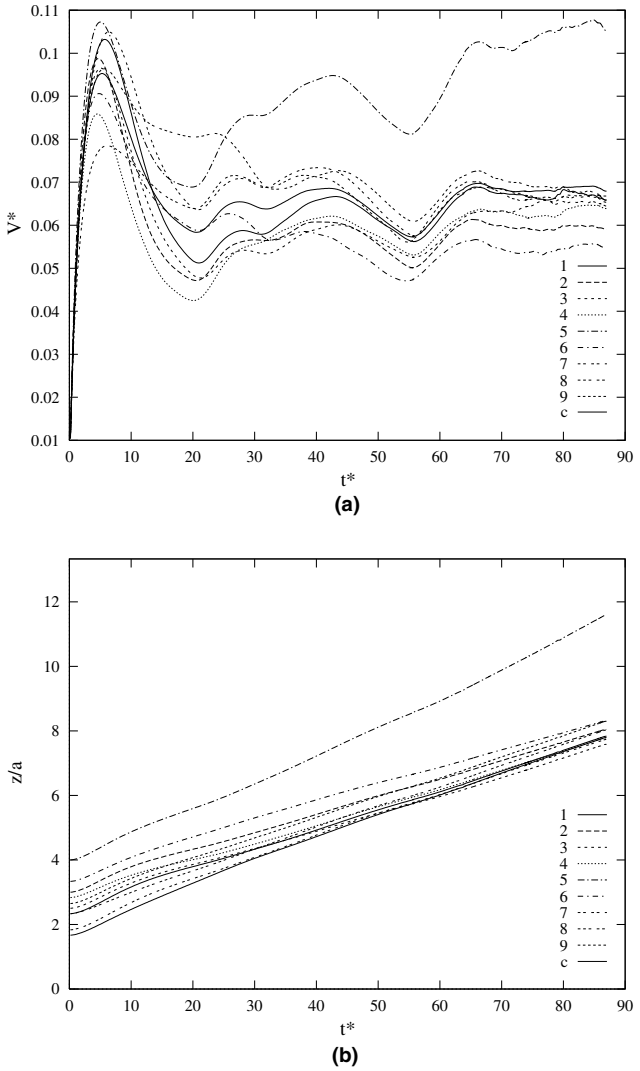

Fig. 8. The nine three-dimensional equal size drop interaction. (a) Migration velocities versus time. (b) z component of the centroid of drops versus time. The non-dimensional numbers are $Re = 5$, $Ma = 20$, $We = 0.0833$ and the material property ratios are 0.5.

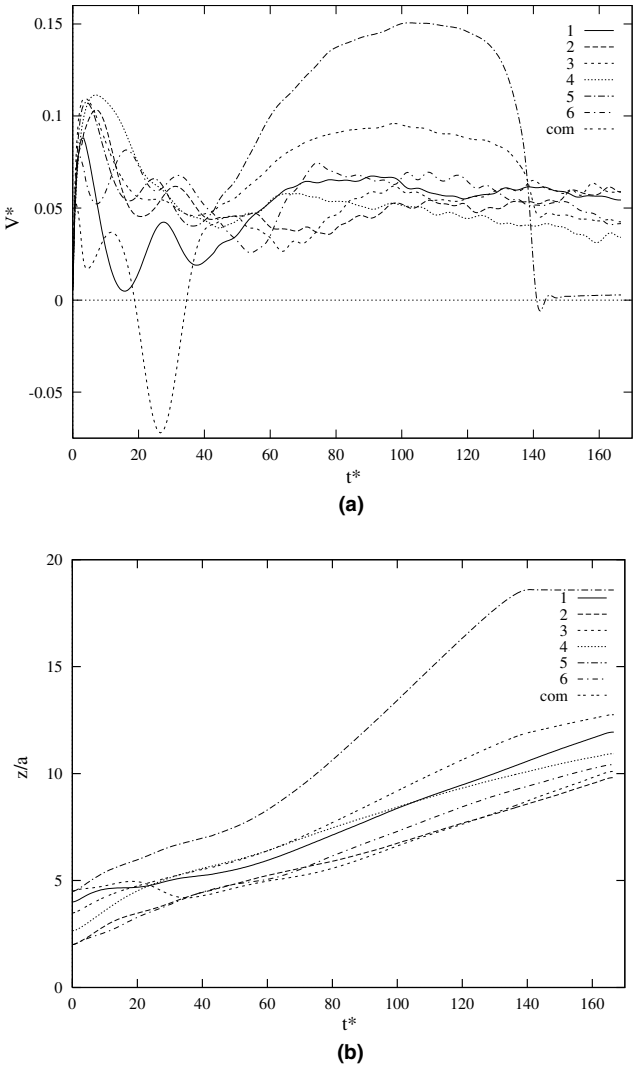

Fig. 10. The six two-dimensional unequal size drop interaction. Drops marked 1–6 from left to right in the domain and "com" denotes the velocity of the center of mass of the drop system. (a) Migration velocities versus time. (b) z component of the centroid of drops versus time.

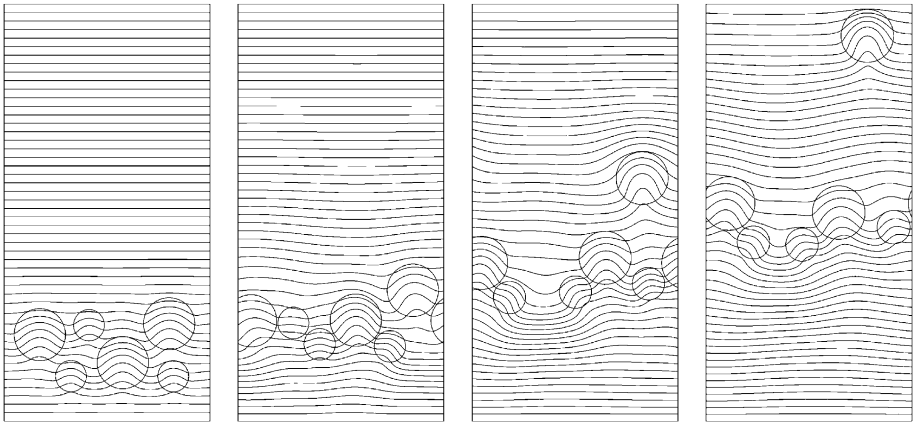

Fig. 9. Isotherms for selected frames from the computation of six two-dimensional unequal size drop interaction. Time progresses from left to right and 50 equally spaced contours are shown. The non-dimensional times (t^*) are 2.5, 25, 87.5, 137.5. Computational domain is $(x/a_v, z/a_v) = (10, 20)$. The non-dimensional numbers based on dimensions of large drops are $Re = 5$, $Ma = 20$, $We = 0.0833$ and the material property ratios are 0.5. The ratio of drop radii is $\lambda = 3/5$.

together and form a nearly horizontal layer at early times. Since the migration velocity of an isolated drop is proportional to the drop radius, it should be expected that small drops move with a lower velocity than big ones. This, however, is only true when the drops are isolated. As seen in these figures, the small drops move very close to the big ones and almost "stick" to the sides of the big drops. It is seen that two big drops collide with the third big one which is ahead of the others. This causes the third drop to separate from the other drops and reach the upper wall well ahead of the others. Although the small drops migrate to the side of the big ones, they together form a nearly horizontal layer across the channel. The reason that the small drops also migrate as fast as the big drops is due to the fact that the small drops are caught in the wake of the large drops. Due to this behavior, the thermal gradient across the small drops is high so their velocities are large. The migration velocity and the vertical location of centroid of each drop are plotted in Fig. 10. The formation of the drop layer can be clearly seen from these figures. The results here are similar to the six-drop simulation in the mono-dispersed case in which once drops fill the channel horizontally, the other drops form a second layer.

As for the mono-dispersed case, a larger system of unequal size drops is also simulated. For this purpose, 16 drops are placed in a domain which extends 13.33 average drop radii in both directions. The number of small drops is selected to be equal to the number of big drops. The resolution is also 256×256 grid points for this case. The ratio of small drop radius to large drop radius is $\lambda = 5/7$. All the other non-dimensional numbers for the big drops are the same as for the previous computations of the 16 mono-dispersed drop case. The interaction of these drops is shown in Fig. 11 where both the drops and the isotherms are illustrated at different time frames. The figure indicates a similar behavior for the ploy-dispersed system to the mono-dispersed case plotted in Fig. 5. As can be seen in the top frames, the drops accelerate quickly and initially move close to each other. Since the sides of the domain are not occupied, initially, the hot ambient fluid flows down there, rather than between the drops. This results in the thermal gradient as seen in Fig. 11. Due to this thermal gradient, some of the leading drops move toward the sides of the domain. As these drops separate from the others, the rest of the drops form a layer, as seen in the bottom frames of the same figure. Because of different drop sizes the layer is not as uniform as for the mono-dispersed case. Nevertheless, this layer across the channel persists until the end of the simulation. The leading drops slow down when they get close to the upper wall and, since the others move faster, eventually all the leading drops come to nearly the same horizontal level before hitting the top wall. The lower layer continues to migrate during this period. The migration velocities plotted in Fig. 12 together with the vertical locations of the drop centroids also show this behavior. The formation of drop layers, until the channel is filled horizontally, is quite similar to the mono-dispersed case.

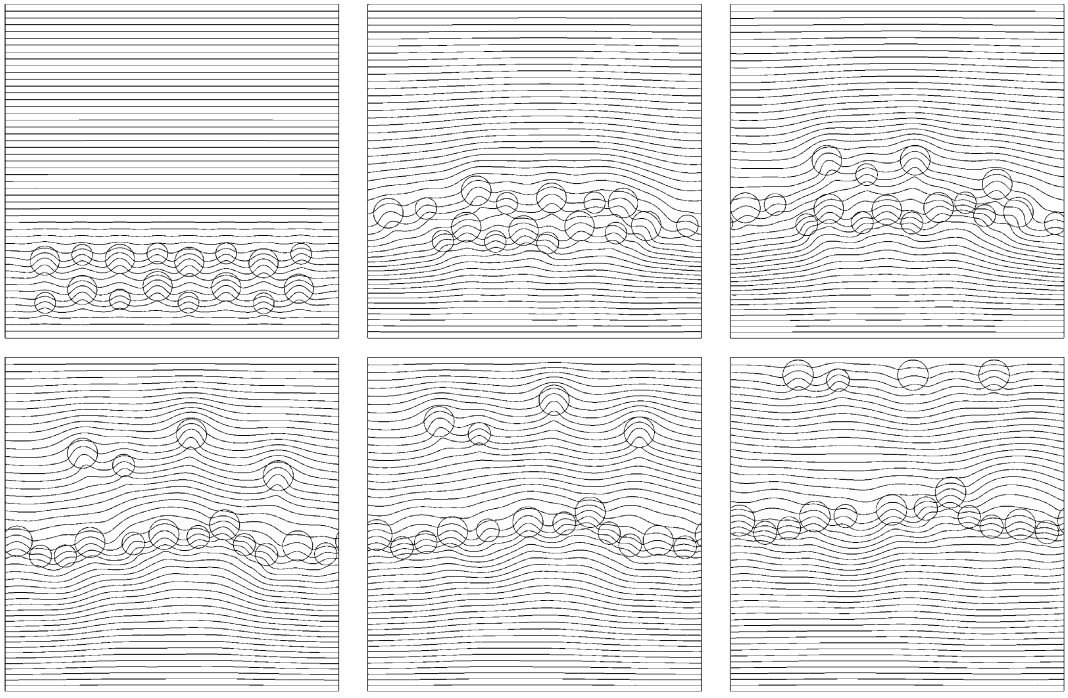

Fig. 11. Isotherms for selected frames from the simulation of 16 two-dimensional unequal size drop interaction. Time progresses from left to right, top to bottom and 50 equally spaced contours are shown. The non-dimensional times (t^*) are 4, 64.7, 89, 137.6, 161.9, 202.4. The computational domain is $(x/a_v, z/a_v) = (13.33, 13.33)$. The non-dimensional numbers based on dimensions of large drops are $Re = 5$, $Ma = 20$, $We = 0.0833$ and the material property ratios are 0.5. The ratio of drop radii is $\lambda = 5/7$.

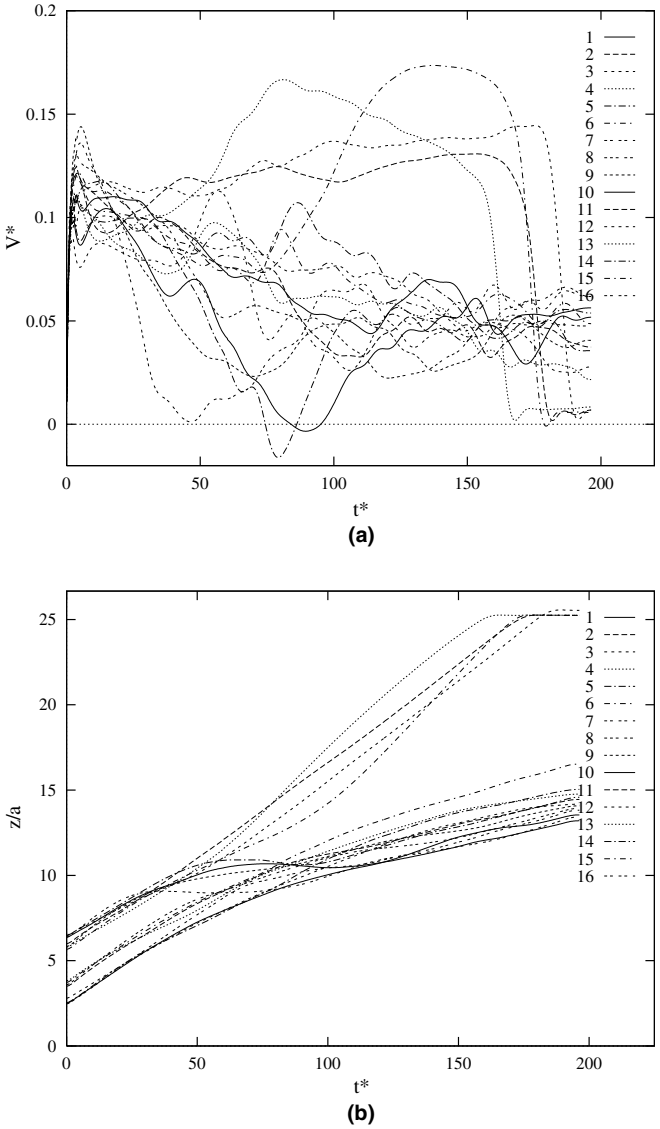

Fig. 12. The 16 two-dimensional unequal size drop interaction. (a) Migration velocities versus time. (b) z component of the centroid of drops versus time. The non-dimensional numbers based on dimensions of large drops are $Re = 5$, $Ma = 20$, $We = 0.0833$ and the material property ratios are 0.5. The ratio of drop radii is $\lambda = 5/7$.

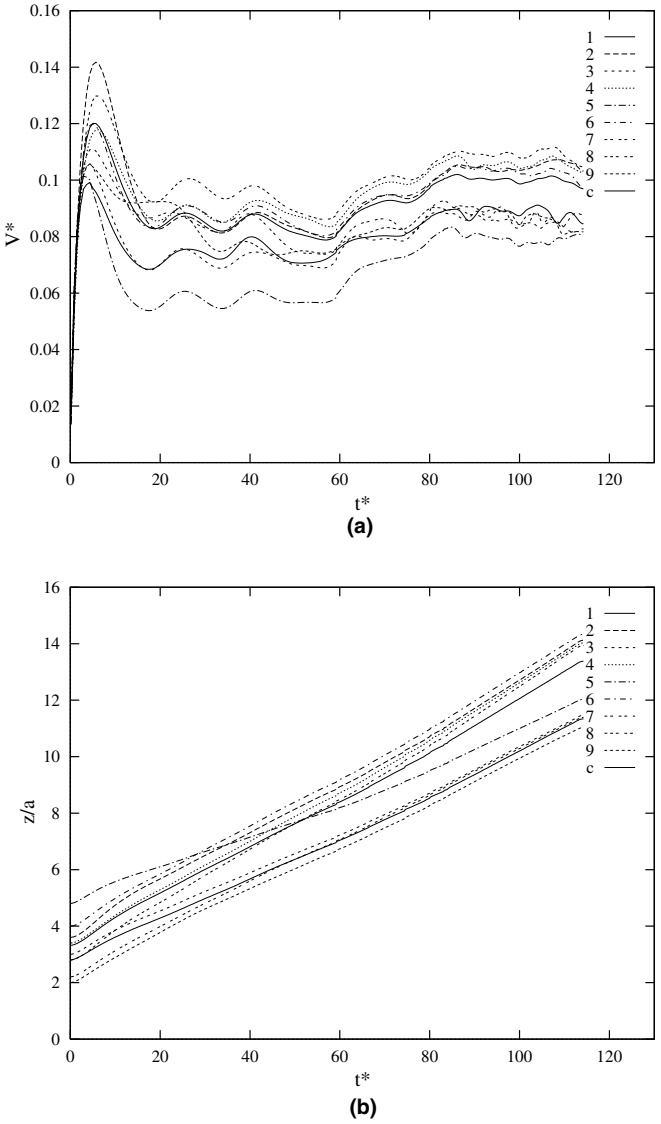

Fig. 13. The nine three-dimensional unequal size drop interaction. (a) Migration velocities versus time. (b) z component of the centroid of drops versus time. Even numbered drops are the larger ones and "c" denotes the center of mass of drop system.

Finally, in order to further verify drop layer formation for real poly-dispersed systems, a fully three-dimensional simulation of unequal size drops is performed. The size of the computational domain is $x/a_v = 8$, $y/a_v = 8$, and $z/a_v = 16$, and it is resolved by a $64 \times 64 \times 128$ grid. The ratio of drop radii is $\lambda = 2/3$. Four big and five small drops are arbitrarily placed close to the lower wall. The non-dimensional numbers based on the dimensions of big drops are the same as in the previous cases. The average drop radius and the average reference velocity are used to scale the quantities computed in this simulation. Since the migration velocity is proportional to the drop radius, the larger drops should migrate faster than the smaller drops and it is not surprising that the larger drops should overtake the rest. This is clearly seen in Fig. 13. The migration velocity of each drop as well as the scaled distance from the centroid of the drops to the lower wall are shown in Fig. 13(a) and (b). In these figures, the drops marked by 2, 4, 6, and 8 correspond to the big drops. The migration velocity of each drop clearly indicates that the larger drops have higher velocities and their migration velocities are similar. The smaller drops also have migration velocities close to each other but each group has a different velocity. Of course, the consequence of this is the two layer formation as observed before. This result confirms that the drop layer formation seen in two-dimensional simulations is also a prominent feature in three dimensional poly-dispersed droplet flows. But, in contrast to the two-dimensional simulations of poly-dispersed system, where the drops of different size form a nearly horizontal layer by migrating close to each other, it is found in three-dimensional simulation of a poly-dispersed system that drops with dif-

ferent sizes form different layers. Each layer moves with a different velocity and the larger the drops, the higher the migration velocity of each layer. This results in a feature that the layer of large drops move as a top layer and the small drops move behind as a lower layer. This is a distinct behavior of three-dimensional simulations of poly-dispersed systems.

4. Conclusions

The behavior of a drop cloud in thermocapillary flows under zero gravity condition is examined both for mono-dispersed and poly-dispersed cases. The numerical simulations of mono-dispersed systems show that the drops form nearly horizontal layers. As soon as the drops form one layer that fills the channel horizontally, the rest of the drops form another layer. Although it is seen in the two dimensional 16-drop simulation that this layer may break up by instability waves, the layer is eventually regenerated. Three-dimensional simulations confirm the formation of drop layers and the simulations of poly-dispersed drop systems show the same behavior. In contrast to two-dimensional simulations of poly-dispersed system, where drops of different size form a horizontal layer, the three-dimensional simulation of a poly-dispersed system shows that drops with different sizes form different layers. Each layer moves with a different velocity and the larger the drops, the higher the migration velocity of each layer. This results in a layer of large drops that moves ahead of a layer of small drops.

Acknowledgements

This study is funded by NASA grants NAG3-1317 and NAG3-2145. Some of the computations have been performed at the Center for Parallel Computing at the University of Michigan and the Center of Excellence for Advanced Engineering Technologies of Istanbul Technical University. We thank Dr. R. Balasubramaniam at NASA Glenn Research Center for valuable discussions.

References

[1] J.L. Anderson, Droplet interaction in thermocapillary motion, Int. J. Multiphase Flow 11 (1985) 813–824.
[2] L.S. Chen, H.J. Keh, The thermocapillary motion of a fluid droplet normal to a plane surface, J. Colloid Interface Sci. 137 (1990) 550–562.
[3] H.J. Keh, S.H. Chen, The axisymmetric thermocapillary motion of two droplets, Int. J. Multiphase Flow 16 (1990) 515–527.
[4] H.J. Keh, S.H. Chen, Droplet interactions in axisymmetric thermocapillary motion, J. Colloid Interface Sci. 151 (1992) 1–16.
[5] H.J. Keh, S.H. Chen, Droplet interactions in thermocapillary migration, Chem. Eng. Sci. 48 (1993) 3565–3582.
[6] M. Meyyapan, W.R. Wilcox, R.S. Subramanian, Thermocapillary migration of a bubble normal to a plane surface, J. Colloid Interface Sci. 83 (1981) 199–209.
[7] M. Meyyapan, R.S. Subramanian, Thermocapillary migration of a gas bubble in an arbitrary direction with respect to a plane surface, J. Colloid Interface Sci. 115 (1987) 206–219.
[8] S. Nas, Computational investigation of thermocapillary migration of bubbles and drops in zero gravity, Ph.D. Dissertation, Department of Aerospace Engineering, The University of Michigan, Ann Arbor, MI, USA, 1995.
[9] S. Nas, G. Tryggvason, Thermocapillary interaction of two bubbles or drops, Int. J. Multiphase Flow 29 (2003) 1117–1135.
[10] R.S. Subramanian, in: R.P. Chabra, D. De Kee (Eds.), The Motion of Bubbles and Drops in Reduced Gravity, Transport Processes in Bubbles, Drops and Particles, Hemisphere Publishing Corp., Washington, DC, USA, 1992, pp. 1–42.
[11] R.S. Subramanian, R. Balasubramaniam, The Motion of Bubbles and Drops in Reduced Gravity, Cambridge University Press, 2001.
[12] G. Tryggvason, B. Bunner, A. Esmaeeli, D. Juric, N. Al-Rawahi, W. Tauber, J. Han, S. Nas, Y.-J. Jan, A front-tracking method for computations of multiphase flow, J. Comput. Phys. 169 (2001) 708–759.
[13] S.O. Unverdi, G. Tryggvason, A front-tracking method for viscous incompressible multiphase flows, J. Comput. Phys. 100 (1992).
[14] N.O. Young, J.S. Goldstein, M.J. Block, The motion of bubbles in a vertical temperature gradient, J. Fluid Mech. 6 (1959) 350–356.
[15] G. Wozniak, J. Siekmann, J. Srulijes, Thermocapillary bubble and drop dynamics under reduced gravity—survey and prospects, Z. Flugwiss Weltraumforsch. 12 (1988) 137–144.
[16] X. Zhang, R.H. Davis, The collision rate of small drops undergoing thermocapillary migration, J. Colloid Interface Sci. 152 (1992) 548–561.